

End-to-end machine-learned interatomic potentials for modeling functionalized mesoporous aluminosilicates

Jong Hyun Jung,^{1,*} Tom Schächtel,^{1,*} Yongliang Ou,^{1,*} Selina Itzigebl,²
Marc Högl,³ Niels Hansen,³ Johanna R. Bruckner,² and Blazej Grabowski^{1,†}

¹*Institute for Materials Science, University of Stuttgart, Pfaffenwaldring 55, 70569 Stuttgart, Germany*

²*Institute of Physical Chemistry, University of Stuttgart, Pfaffenwaldring 55, 70569 Stuttgart, Germany*

³*Institute of Thermodynamics and Thermal Process Engineering,
University of Stuttgart, Pfaffenwaldring 9, 70569 Stuttgart, Germany*

(Dated: December 3, 2025)

The structural hierarchy and chemical flexibility of metallosilicates enable broad technological applications, yet they also make it challenging to uncover structure–property relations. Previous large-scale atomistic simulations have provided mechanistic insight, but their accuracy and achievable model complexity remain constrained by the available interatomic potentials. Here, we present an end-to-end workflow for developing accurate and efficient machine-learning potentials, specifically moment tensor potentials (MTPs), tailored for structurally and chemically complex systems such as metallosilicates. The workflow integrates *de novo* structure generation, surface functionalization, and property evaluation. A domain-specific training strategy is employed: Configurations associated with melt–quench generation and subsequent functionalization train the *syn-MTP*, whereas configurations near equilibrium train the *eq-MTP*. We apply the workflow to prototypical metallosilicates, i.e., aluminosilicates, which we also experimentally synthesize and characterize for benchmarking the simulations. The *syn-MTP* reliably generates amorphous aluminosilicates that match experimental density and pair distribution functions measured with synchrotron X-ray diffraction. The *eq-MTP* reproduces experimental infrared spectra and surface hydroxyl densities, along with density-functional-theory-derived dehydrogenation energies, demonstrating meta-GGA-level accuracy and validating the end-to-end workflow. Finally, we showcase the applicability of the developed potentials by predicting infrared spectra of functionalized porous aluminosilicates. This study establishes a robust path toward accurate modeling of realistic metallosilicates under *operando*-relevant conditions.

INTRODUCTION

Metallosilicates represent a versatile class of materials with broad applications in catalysis,¹ separation,² sensing,³ and energy technologies.⁴ These materials feature a structural hierarchy—from amorphous network topology and micro-meso-porosity to particle-scale grains—enabling tunable adsorption properties.^{5,6} In parallel, their high chemical flexibility, including incorporation of various transition metals, adjustable metal loading, and tailored surface functionalization, provides controlled interfacial acidity and catalytic activity.^{7,8} Yet, systematic experimental investigation across this vast structural–chemical design space remains costly and time-consuming.

Atomic-scale modelling provides a powerful mechanistic route to uncover structure–property relations and accelerate the informed development of metallosilicates. Reliable atomistic simulations, however, require access to highly accurate potential-energy surfaces. Electronic-structure methods within the density functional theory (DFT) framework deliver such accuracy but are computationally prohibitive for large models and for extracting kinetic information through molecular dynamics (MD).^{41,42} Empirical force fields, such as ReaxFF,⁴³ calibrated against experimental or *ab initio* data, enable large-scale MD but often fail to describe multicomponent systems due to their fixed functional forms.⁴⁴ On the other hand, recently developed high-dimensional foundation models, such as GRACE,⁴⁵ show promising transferability across broad chemical spaces. Still, their accuracy remains constrained by the quality and diversity of the available train-

ing data, which predominantly consist of near-equilibrium configurations.^{46,47} Therefore, uncertainties grow for reactive events involving transition states or substantial bond rearrangements, further compounded by the utilized convergence parameters and exchange–correlation functionals (commonly Perdew–Burke–Ernzerhof, PBE^{46,47}) that underrepresent dispersion interactions.^{48,49} Fine-tuning and uncertainty quantification are also non-trivial owing to the high dimensionality of the parameter space.⁵⁰ Lightweight machine-learning interatomic potentials (MLIPs) tailored to the targeted structural and chemical domains enriched by active learning offer a practical alternative: They require comparatively small training sets owing to moderate model complexity, enable high-fidelity reference calculations, and remain accurate and computationally efficient for large-scale MD.

The key to developing lightweight MLIPs lies in constructing suitable training datasets. The dataset must be rigorously curated to remain both representative and of manageable size, as excessive growth may ultimately compromise accuracy and training efficiency. For metallosilicates, most available MLIPs targeted relatively simple structures (cf. previous studies in Table I), although complex motifs—such as ordered mesoporosity and surface functionalization—are essential for realistic applications.^{51,52} Developing MLIPs capable of describing such motifs is hindered by several factors: (i) *a priori* mesopore-containing atomic models are generally unknown, requiring *in silico* construction; (ii) the presence of reactive chemistries, where the underlying mechanisms remain largely unexplored; and (iii) the need to validate the chosen exchange–correlation functional, given the strong dispersion interactions in metallosilicates. Further, schemes integrating MLIP development and validation against experimentally measurable properties—rather than relying solely on regression metrics—for metallosilicates are still lacking, restricting the predictive reliability of prior simulation results (Table I).

* These authors contributed equally to this work.

† blazej.grabowski@imw.uni-stuttgart.de

TABLE I. Overview of prior studies developing *ab initio*-based machine-learning interatomic potentials (MLIPs) from density-functional theory (DFT) data. Studies on systems related to silicon examining structural motifs—including amorphous matrix, ordered mesoporosity, surface functionalization, and interfacial water—are summarized. The present work extends prior studies by addressing a broader and more complex range of structural motifs.

Year	System	XC functional ^a	MLIP ^b	Structural motif				Ref.
				Amorphous matrix	Ordered mesoporosity	Surface functionalization	Interfacial water	
2018	Si	PW91	GAP	x				[9]
2018	Si–O	PBE	GMM	x				[10]
2021	Si–Ca–O–H	PBE	BPNN				x	[11]
2022	Si–B–O–F	PBE	DeePMD	x				[12]
2022	Si–O	SCAN	GAP	x				[13]
2022	Si–H	PBE	GAP	x				[14]
2024	Si–Na–O	PBE	DeepPot-SE	x				[15]
2024	Si–O	SCAN	ACE	x				[16]
2024	Si–Al–O–H ^c	SCAN-D3(BJ), ω B97X-D3(BJ)	SchNet				x	[17]
2024	Si–H–O	PBE	DeePMD	x			x	[18]
2024	oxide glass ^d	PBEsol	DeepPot-SE	x				[19]
2024	Si–C–O	SCAN	ACE	x				[20]
2024	Si–C–O–H	PBE	MTP	x				[21]
2024	Si–O–H	ω B97X-D3	PaiNN				x	[22]
2025	Si–Al–O–H	r ² SCAN-D4, vdW-DF-cx	MTP	x	x	x	x	this work

^a Generalized gradient approximation (GGA) exchange–correlation (XC) functionals include Perdew–Wang (PW91),²³ Perdew–Burke–Ernzerhof (PBE),²⁴ and revised PBE for solids (PBEsol).²⁵ The semilocal functionals strongly constrained and appropriately normed (SCAN)²⁶ and regularized–restored SCAN (r²SCAN)²⁷ are included. A study used an empirical dispersion correction D3(BJ) with SCAN²⁸ and range-separated hybrid GGA functional with nonlocal correlation (ω B97X).²⁹ In the present study, r²SCAN with empirical dispersion correction D4³⁰ and the nonlocal Van der Waals functional vdW-DF-cx³¹ were used.

^b Gaussian approximation potential (GAP),³² Gaussian mixture model (GMM),³³ Behler–Parrinello neural network potential (BPNN),³⁴ deep potentials (DeePMD),³⁵ deep potentials smooth edition (DeepPot-SE),³⁶ atomic cluster expansion (ACE),³⁷ SchNet,³⁸ polarizable atom interaction neural network (PaiNN),³⁹ moment tensor potential (MTP)⁴⁰ were used.

^c Proton-exchanged aluminosilicate zeolites.

^d With eight components: SiO₂–Al₂O₃–B₂O₃–Na₂O–CaO–MgO–ZrO₂.

Herein, we propose a comprehensive workflow for developing MLIPs tailored to structurally and chemically complex systems such as metasilicates. The workflow is computationally efficient and broadly applicable, enabled by integrating end-to-end machine-learning with domain-specific training. To generate training datasets, iterative active learning is embedded within the end-to-end modeling of a targeted system, spanning *de novo* structure generation, functionalization, and property evaluation. We introduce a complementary MLIP training and utilization strategy in which multiple MLIPs are optimized to capture distinct domains of the potential-energy surface. High-energy configurations, essential for *in silico* construction and functionalization, are separated from near-equilibrium ones, ensuring that each modeling stage is described by an accurate MLIP.

We apply the proposed workflow to develop moment tensor potentials (MTPs) for ordered mesoporous aluminosilicates (SiO₂–Al₂O₃), which possess enhanced hydrothermal stability and strong Brønsted acid sites.⁷ The resulting datasets span a wide configurational space, covering variations in Al/Si ratio, surfaces, pores, functional groups, water, and interfaces, labeling with dispersion-aware functionals. We demonstrate the application of the obtained efficient and accurate potentials through a combined experiment–simulation study. MTP-accelerated simulations can closely replicate the experimental synthesis, allowing atomic-level resolution of crucial struc-

tural features. The accuracy of both the MTPs and simulated results is rigorously validated against experimental data, including bulk densities, pair distribution functions (PDFs), vibrational spectra, and functional group densities. Finally, we show that these potentials can predict key phenomena, such as infrared spectra of functional groups at the pore surface, which are critical for optimizing mesoporous aluminosilicate performance.

RESULTS

End-to-end learning and modeling

The proposed end-to-end modeling workflow is presented in Fig. 1. The workflow starts from precursors, resolves the bulk and surface structures of mesoporous aluminosilicates, and predicts experimentally measurable properties with near-*ab initio* accuracy, by combining MTPs with large-scale MD simulations. A domain-specific MTP training strategy is integrated to complement the end-to-end workflow, delivering accuracy and efficiency across all stages of modeling.

The generation of a realistic atomistic structure of mesoporous aluminosilicates with functionalized –OH groups is based on MD simulations accelerated by a synthesis-stage MTP (*syn-MTP*). To cover the full synthesis and functional-

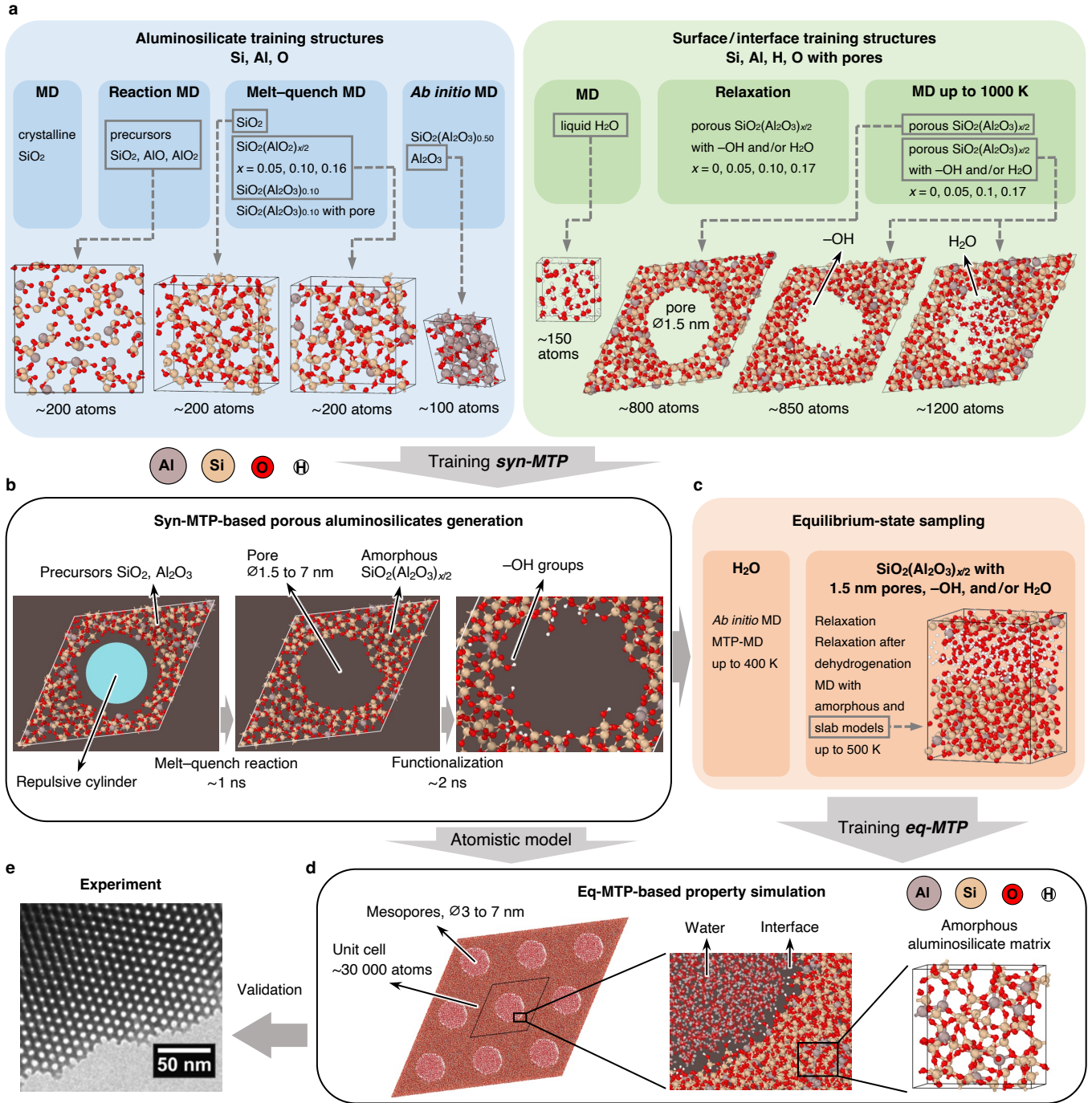


FIG. 1. Development of accurate and efficient MLIPs via end-to-end machine-learning and domain-specific training for modeling functionalized mesoporous aluminosilicates with confined water. **a**, Generation of the syn-MTP training set. The dataset includes both bulk aluminosilicate and pore configurations. Amorphous aluminosilicates are generated *in silico* by molecular dynamics (MD) simulations of precursor reactions and melt-quench procedures of silica-alumina mixtures. Active learning is performed in MD with syn-MTP to explore the complex configurational space. Additional structures are obtained from *ab initio* MD. To describe aluminosilicate interacting with water, liquid water and H_2O -aluminosilicate interface structures are included. MD simulations with active learning are conducted up to 1000 K to further enrich the dataset. **b**, Resolving the realistic porous aluminosilicate structures obtained from experiments using syn-MTP. An artificial repulsive potential is applied to define a one-dimensional pore, followed by precursor filling and melt-quench amorphization. After the removal of repulsive potential, the pore surface is functionalized with hydroxyl ($-\text{OH}$) groups using syn-MTP. **c**, Generation of the eq-MTP training set via equilibrium-state sampling. MD-driven active learning up to 400 K is used to sample water-infiltrated porous aluminosilicates, as well as slab and dehydrogenated structures. **d**, Large-scale MD simulations of realistic mesoporous aluminosilicates interacting with water. The trained lightweight yet accurate eq-MTP enables efficient prediction of target material properties. Some water molecules at the interface are not visualized to highlight the surface $-\text{OH}$ groups. **e**, Experimental characterization of the synthesized mesoporous aluminosilicates, providing quantitative validation of the trained MTPs. Upon validation, the eq-MTP can be applied to predict a wide range of properties of mesoporous aluminosilicates. A representative transmission electron microscopy image of the synthesized mesoporous silica is shown.

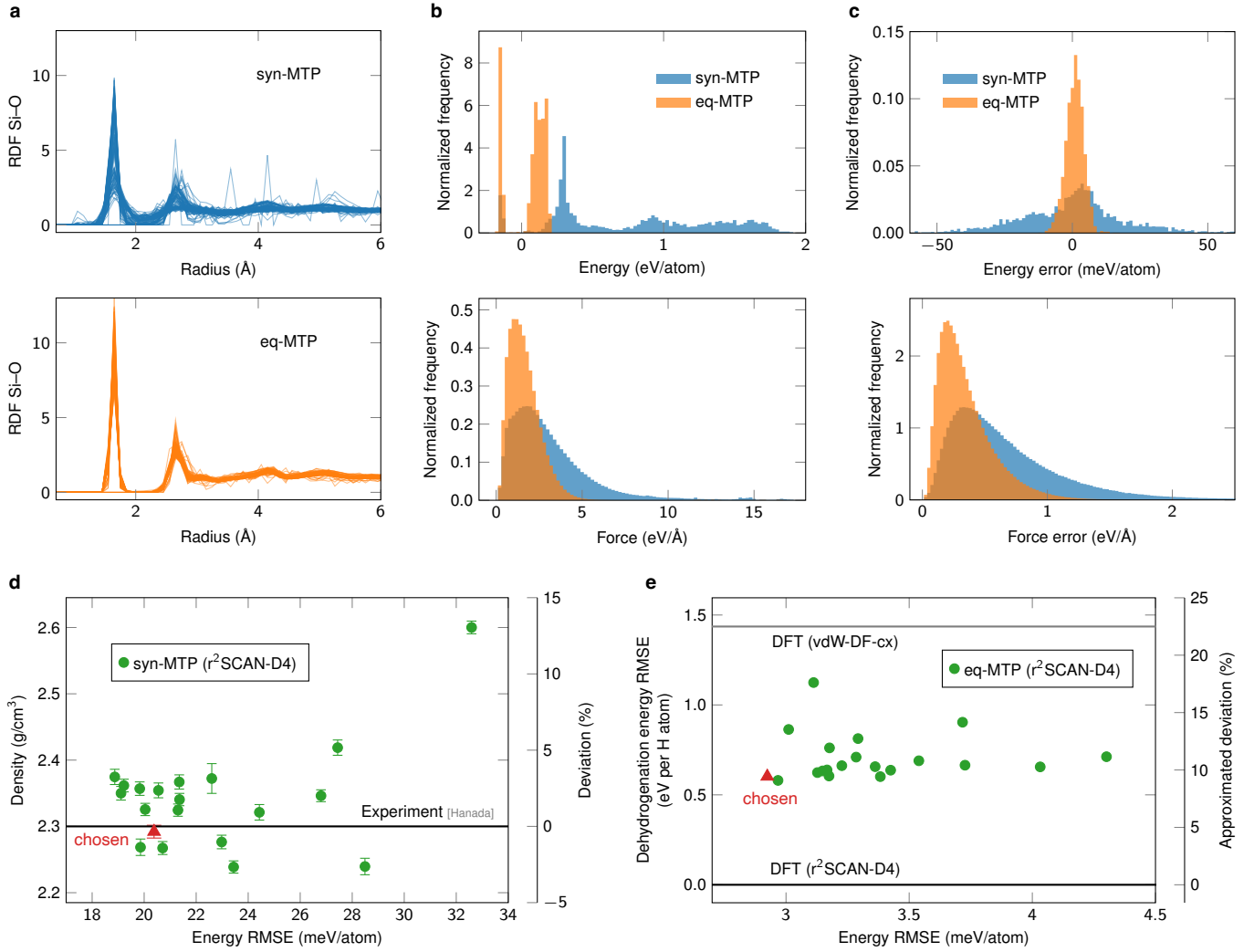


FIG. 2. Training datasets and training of syn-MTP and eq-MTP based on the r^2 SCAN-D4 functional. **a**, Radial distribution functions (RDFs) of Si-O pairs in 100 randomly selected configurations in the corresponding training datasets. The syn-MTP configurations exhibit greater variation in the RDFs, reflecting the broader structural diversity required to describe the synthesis processes. **b**, Distribution of energies and force norms from DFT calculations for all configurations in the training datasets. Energies are referenced to the 0 K relaxed energies of α -quartz (SiO_2), α -alumina (Al_2O_3), a H_2O molecule, and an O_2 molecule in vacuum. The syn-MTP training set spans a broader range of relative energies and atomic forces. **c**, Distributions of training errors in energy and force vector, given as deviations of MTP predictions from DFT values. For both energy and force, more configurations in the training set of syn-MTP show a larger training error. **d**, Predicted densities of bulk amorphous aluminosilicate at 300 K with an Al/Si molar ratio of 0.17, obtained from ensemble syn-MTP candidates trained on the same dataset. The error bars represent the 95% confidence intervals from multiple melt-quench runs. The syn-MTP with density closest to the experiment value from Hanada⁵³ and a relatively low root-mean-square error (RMSE) was selected for production runs. **e**, RMSE in dehydrogenation energy at 0 K for ensemble eq-MTP candidates fitted to the same training set. The eq-MTP exhibiting low RMSE in both training and dehydrogenation energies was chosen for predictive simulations. The final eq-MTP achieves an average relative deviation of $\sim 10\%$ in the dehydrogenation energy, less than the RMSE for the dehydrogenation energies between r^2 SCAN-D4 and an available ReaxFF potential,⁴³ 1.98 eV.

ization process, the syn-MTP must be trained on a broad configuration space (Fig. 1a). The sampling of aluminosilicate environments in the configuration space starts from four regions: (i) crystalline SiO_2 bulk phases; (ii) chemical reactions starting from multiple molecular SiO_2 , AlO , and AlO_2 units placed in the simulation cell; (iii) melt-quenching of SiO_2 and silica-alumina mixtures up to 6000 K to generate amorphous structures; and (iv) additional *ab initio* MD for amorphous and crystalline Al_2O_3 to capture configurations associated with Al incorporation. To describe mesopore environments and water chemistry, the training set also includes configurations containing liquid water, $-\text{OH}$ functionalized pore

surfaces, and water-filled mesopores. During MTP-based MD, on-the-fly active learning is employed to automatically expand the training set in poorly sampled regions of configuration space. In total, the training set consists of 3185 configurations (8.7×10^5 atoms), for which energies, forces, and stresses from DFT calculations are used to fit the syn-MTP.

Starting from precursors, we resolve the experimentally synthesized amorphous aluminosilicates using an *in silico* synthesis protocol in analogy to experimental processing (Fig. 1b). Precursor molecules SiO_2 and Al_2O_3 are placed in the simulation cell according to the target Al/Si ratio to generate the amorphous aluminosilicate matrix. Mesopores are

TABLE II. **Training RMSE of the domain-specific MTPs.** MTPs of level 16 with 608 fitting coefficients were used. Four elements (Si, O, Al, H) were fitted with the maximum neighbor distance of 5 Å. The values inside brackets show the maximum values in the corresponding ensemble candidates of trained MTPs. The eq-MTP exhibits substantially lower training errors than the syn-MTP in all energy, force, and stress.

XC functional	Domain	#Configurations	#Atoms (10^6)	Energy (meV/atom)	Force ^a (eV/Å)	Stress (GPa)
vdW-DF-cx	syn-MTP	3185	0.87	15.7 (24.7)	0.802 (0.914)	1.58 (3.08)
vdW-DF-cx	eq-MTP	4331	3.35	3.0 (3.64)	0.392 (0.432)	0.20 (0.50)
r ² SCAN-D4	syn-MTP	3185	0.87	20.4 (32.6)	0.928 (1.231)	2.16 (4.52)
r ² SCAN-D4	eq-MTP	4395	3.40	3.3 (4.30)	0.429 (0.473)	0.29 (0.54)

^a RMSE of lengths of force vectors.

introduced by applying a repulsive Lennard–Jones potential based on the distance to the center of a cylinder extended thoroughly along the cell’s z -axis, preventing atoms from occupying the pore region and thereby defining the pore size by the cutoff of the potential. A melt–quench MD protocol of 1 ns is then used to synthesize the amorphous matrix with controlled mesoporosity. Subsequently, a functionalization step is carried out by introducing –OH groups on the pore surfaces and relaxing the structure using syn-MTP. Finally, the system is equilibrated at 300 K, and any H₂O molecules formed from unstable –OH groups are removed to yield a stable, functionalized mesoporous aluminosilicate structure.

Since syn-MTP is trained to cover a broad configuration space, its accuracy near equilibrium is inherently limited. To obtain a high-accuracy potential for equilibrium and near-equilibrium structures, we generated a new training set using syn-MTP-based MD sampling focused on the targeted systems (amorphous and hydrated mesoporous aluminosilicates, Fig. 1c) at relatively low temperatures (up to 500 K). The sampling is enriched via active learning with a reduced extrapolation threshold (e.g., 2, compared to 5 used for syn-MTP) to concentrate on well-relaxed configurations. Including slab geometries in the training set improves the stability of the resulting potential without significantly increasing the training error. Configurations with maximum force norms exceeding 10 eV/Å are considered far from equilibrium and excluded. Single-point DFT calculations are then performed for the remaining structures (about 4300 configurations, 3.4×10^6 atoms), and the resulting energies, forces, and stresses constitute the training dataset for the equilibrium-stage potential, *eq-MTP*.

With eq-MTP, realistic structures can be simulated on long time scales, yielding predictions that are quantitatively comparable to experimental measurements (Fig. 1d). In the present study, mesoporous aluminosilicates with amorphous matrices are synthesized and characterized experimentally, providing a direct basis for validating the end-to-end modeling workflow and confirming the accuracy of the resulting MTPs (Fig. 1e).

Training of domain-specific MTPs

To highlight differences in the local atomic environments of the two training datasets, 100 configurations were randomly selected from each dataset. The respective radial distribution functions of Si–O pairs are visualized in Fig. 2a. Compared to the equilibrium-state configurations, the dataset from the synthesis process exhibits greater variation in Si–O bond lengths, reflecting more diverse local environments. This is further re-

flected in the energies and atomic forces of the configurations (Fig. 2b): the synthesis dataset includes configurations with relative energies up to 1.8 eV/atom, whereas equilibrium configurations reach only 0.3 eV/atom. Correspondingly, forces as large as 15 eV/Å appear in the synthesis dataset, while most forces in equilibrium remain within 5 eV/Å. These results indicate that the melt–quench and functionalization processes sample configurations far from equilibrium, whereas predicting material properties near room temperature requires only configurations close to equilibrium.

Under the domain-specific training strategy, two datasets generated from the synthesis process and equilibrium states in the end-to-end modeling workflow were used to train syn-MTP and eq-MTP, respectively. Both MTPs were trained with the same model complexity (number of fitting coefficients) but tailored to different domains of phase space and applications. The training errors are shown in Fig. 2c. Syn-MTP exhibits higher fitting errors, with energies as large as ± 50 meV/atom and forces more than 2 eV/Å, whereas eq-MTP shows much lower errors, with energies mostly within ± 10 meV/atom and forces mostly within 1 eV/Å. These results demonstrate that the domain-specific training strategy enhances the accuracy of the potentials without increasing their complexity.

To investigate the MTP parameter space, we performed independent training multiple times with varying random seeds and on the same synthesis and equilibrium datasets, thereby generating ensembles of syn-MTP and eq-MTP candidates, respectively. The quality of the syn-MTP candidates is evaluated based on the critical amorphous materials property—density of bulk amorphous aluminosilicates (Fig. 2d). The training errors in energy ranging from 18 meV/atom to 33 meV/atom result in the uncertainties of 2.2 g/cm³ to 2.6 g/cm³ in the predicted density, which corresponds to errors of up to 13 % relative to the experimental value (about 2.3 g/cm³).⁵³ Within this ensemble, the MTP with the lowest training error does not yield a density in close agreement with the experiment. Therefore, for further validation, another MTP was chosen; the one reproducing the experimental density and having a relatively small training error.

Dehydrogenation at mesoporous surfaces is an important chemical process relating to surface acidity, yet resolving the energetics of this process at different atomic sites is challenging in experiments.^{58–61} We therefore examine the quality of the eq-MTP with dehydrogenation energies against DFT (Fig. 2e). The eq-MTP training errors of 2.9 meV/atom to 4.4 meV/atom lead to errors of 0.5 eV per H atom to 1.1 eV per H atom in the dehydrogenation energy, corresponding to approximately 9 % to 17 % deviation. The relatively large deviation in dehydrogenation energy

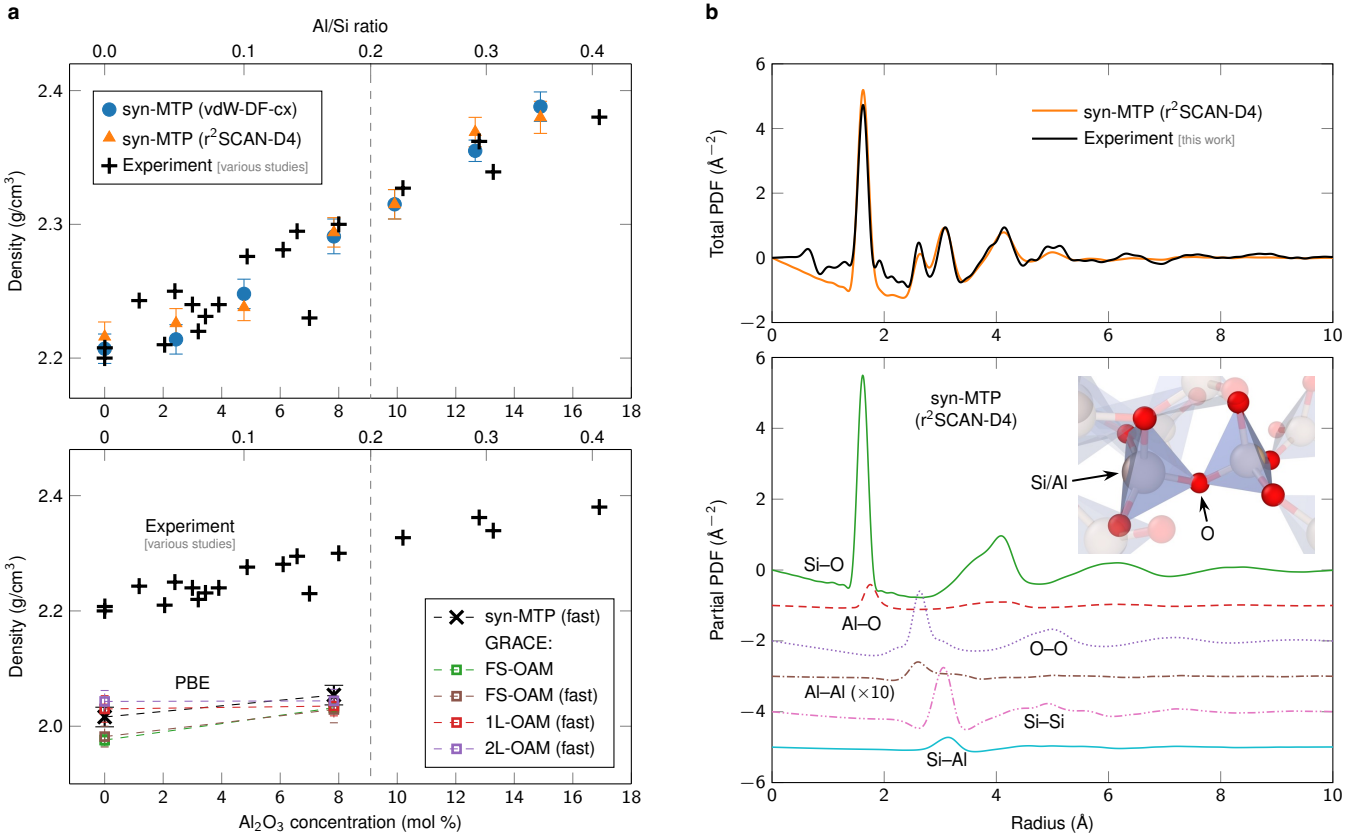


FIG. 3. Validation of syn-MTP on bulk amorphous aluminosilicates. **a**, Comparison of aluminosilicate densities at 300 K as a function of Al_2O_3 concentration between simulation and experiment. Experimental data are taken from Ando,⁵⁴ Morikawa,⁵⁵ Khemis,⁵⁶ Hanada,⁵³ and Ohira.⁵⁷ The syn-MTPs trained to both exchange–correlation functionals (vdW-DF-cx and $r^2\text{SCAN-D4}$) agree well with the experimental values. GRACE models⁴⁵ trained to the PBE functional underestimate the density by about 10%. For comparison, a syn-MTP trained to PBE shows results consistent with the GRACE model. Error bars indicate the 95% confidence intervals from multiple melt–quench simulations. **b**, Comparison of pair distribution functions (PDFs) for aluminosilicate with a molar Al/Si molar ratio of 0.2 at 300 K. Atomic model synthesized *in silico* with syn-MTP reproduces experimental total PDFs accurately. Partial PDFs derived from simulations are also shown, offering atomic insights in aluminosilicates.

stems from the high atom count of the model (~ 700 atoms) necessary for constructing the pores. Nevertheless, these errors remain smaller than those introduced by the choice of exchange–correlation functional. For example, switching the functional from $r^2\text{SCAN-D4}$ to vdW-DF-cx changes the DFT dehydrogenation energy by about 23 %. From the eq-MTP ensemble, we select the one with the lowest errors in both training and dehydrogenation-energy predictions for subsequent validations. Overall, our findings demonstrate that errors in training and targeted properties are not directly correlated, underscoring the need for explicit validation of MLIPs before large-scale applications.

Details on the training sets and the overall errors are provided in Table II. To assess the influence of the exchange–correlation functional, we developed MTPs using two types of functionals: $r^2\text{SCAN-D4}$, which includes empirical dispersion, and the nonlocal vdW-DF-cx. The eq-MTPs of both functionals achieve substantially lower errors—notably about fivefold in energy, twofold in forces, and eightfold in stress—highlighting their improved accuracy.

Validation of end-to-end modeling and MTPs

We have demonstrated that training error alone is insufficient to validate MTPs fitted to *ab initio* data. To validate the accuracy of MTPs learned via end-to-end modeling, we perform experimental synthesis of bulk and mesoporous aluminosilicates in parallel with *in silico* synthesis using syn-MTPs. Observations from experiments are then compared with results extracted from large-scale MD simulations accelerated by eq-MTP, based on the atomic models generated by syn-MTP.

For syn-MTP, the *in silico*–synthesized bulk aluminosilicates with varying Al/Si ratios are benchmarked against experimental values reported in multiple prior studies (Fig. 3a). The predicted densities obtained using both functionals—vdW-DF-cx and $r^2\text{SCAN-D4}$ —are consistent with each other and quantitatively reproduce experimental values for aluminosilicates with Al incorporation up to 30%. In contrast, the GRACE model, when applied to the same *in silico* synthesis protocol, systematically underestimates the density by roughly 10% (2.0 compared with 2.2 for silica). We further developed a syn-MTP trained on DFT data computed with the PBE functional, and this syn-MTP yields densities consistent with the GRACE predictions. These results indicate that functionals incorporating explicit vdW interactions are necessary to cap-

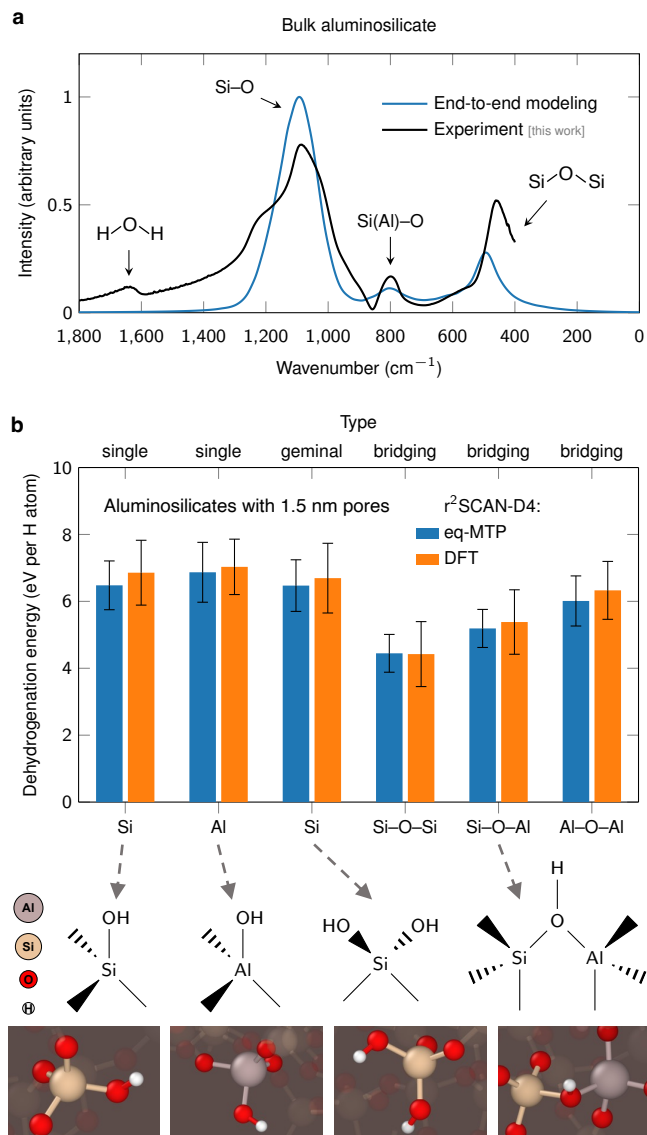


FIG. 4. Validation of the end-to-end modeling workflow and eq-MTP. **a**, Comparison of the infrared spectrum of bulk amorphous aluminosilicate with the Al/Si molar ratio of 0.05 predicted by eq-MTP and measured experimentally. Syn-MTP and eq-MTP trained on r^2 SCAN data were employed in the end-to-end modeling workflow. The close match of the characteristic Si-O-Si peak confirms the accuracy of both the r^2 SCAN-D4 functional and eq-MTP. **b**, Comparison of dehydrogenation energies at 0 K predicted by eq-MTP and DFT. Dehydrogenation was modeled at the surfaces of pores with a diameter of 1.5 nm in *in silico*-synthesized aluminosilicate with an Al/Si molar ratio of 0.2. Error bars represent the standard deviation arising from multiple hydrogen sites on the pore surface. The agreement demonstrates that eq-MTP retains near-*ab initio* accuracy. Dehydrogenation energies are similar for the single and geminal hydroxyl groups and generally lower for the bridging hydroxyl groups. Illustrative structural formulas and atomic sites for different types of dehydrogenation are shown.

ture aluminosilicate densities within DFT.

While density is an averaged property, we further validate the syn-MTP accuracy for local atomic environments by comparing predicted PDFs with experimental data obtained from the present study (Fig. 3b). Bulk aluminosilicate powders with a molar Al/Si molar ratio of 0.2 were synthesized, and total scattering measurements performed at the European

Synchrotron Radiation Facility were used to obtain experimental PDFs. In parallel, MD simulations with syn-MTP at 300 K were performed using the *in silico*-synthesized atomic model with the same Al/Si ratio, and simulated PDFs were extracted from MD snapshots. We show that simulations accurately reproduce the peaks in total PDFs observed experimentally, demonstrating that the *in silico*-synthesized models capture the local structure of experimentally synthesized samples. These results confirm the high accuracy of syn-MTP and support the validity of the proposed *in silico* synthesis workflow. Furthermore, decomposition of the simulated PDFs provides element-resolved structural information that is inaccessible experimentally. The so assigned peaks match well with previously reported zeolite positions,^{62–64} which further validates the simulated atom positions. Since Al-related features overlap with those of other atoms, varying the Al concentration is not expected to strongly affect the total PDF profile.

Vibrational properties at finite temperatures provide a quantitative validation of the melt-quench-generated structures and the near-equilibrium potential-energy surface described by eq-MTP. Experimentally, Fourier-transform infrared spectroscopy was used to obtain the infrared spectrum of bulk amorphous aluminosilicate with an Al/Si molar ratio of 0.05. In the end-to-end modeling workflow, MD simulations with eq-MTP were performed on atomic models synthesized by syn-MTP to extract an effective harmonic potential, from which infrared spectra were obtained via polarization calculations under the DFT framework. Figure 4a shows that infrared spectra predicted by the proposed end-to-end modeling workflow accurately reproduce the main vibrational bands at 1100 cm^{-1} (Si-O antisymmetric stretching) and 400 cm^{-1} (Si-O-Si bending),⁶⁵ confirming the high accuracy of the workflow accelerated by domain-specific MTPs. Discrepancies above 1200 cm^{-1} are attributed to unavoidable residual water in the experimental samples, as indicated by the characteristic scissoring band of water near 1600 cm^{-1} .⁶⁶

We validate the accuracy of the eq-MTP in describing reaction energetics associated with different dehydrogenation pathways at pore surfaces in aluminosilicates. Dehydrogenation energies computed using eq-MTP and DFT for aluminosilicates with an Al/Si molar ratio of 0.2 and 1.5 nm pore diameter are compared in Fig. 4b. For each dehydrogenation type, at least 37 distinct surface sites are sampled to obtain statistics. The close agreement between eq-MTP and DFT highlights the near-*ab initio* accuracy of eq-MTP. Among the examined environments, the bridging Si-OH-Si hydroxyl group exhibits the lowest dehydrogenation energy (about 4.5 eV per H atom), indicating that it is the most energetically favorable site for hydrogen removal. Dehydrogenations of single and geminal hydroxyl groups show similar energetics, both around 7 eV per H atom. These values are close to the O-H bond dissociation energy predicted for silanol (about 5.2 eV per H atom).⁶⁷

The modeled aluminosilicates with a pore diameter of 6.1 nm, obtained after functionalization and annealing, exhibit a total hydroxyl surface density of 1.5 nm^{-2} , in close agreement with experimental measurements (1.6 nm^{-2}).⁶⁸ The surface density of bridging Si-(OH)-Al hydroxyl groups is predicted to be 0.13 nm^{-2} , near the experimentally determined value (0.08 nm^{-2})⁶⁸ for Brønsted acid sites. This discrepancy likely arises from the limited sensitivity of the experimental pyridine-infrared method in detecting weak Brønsted

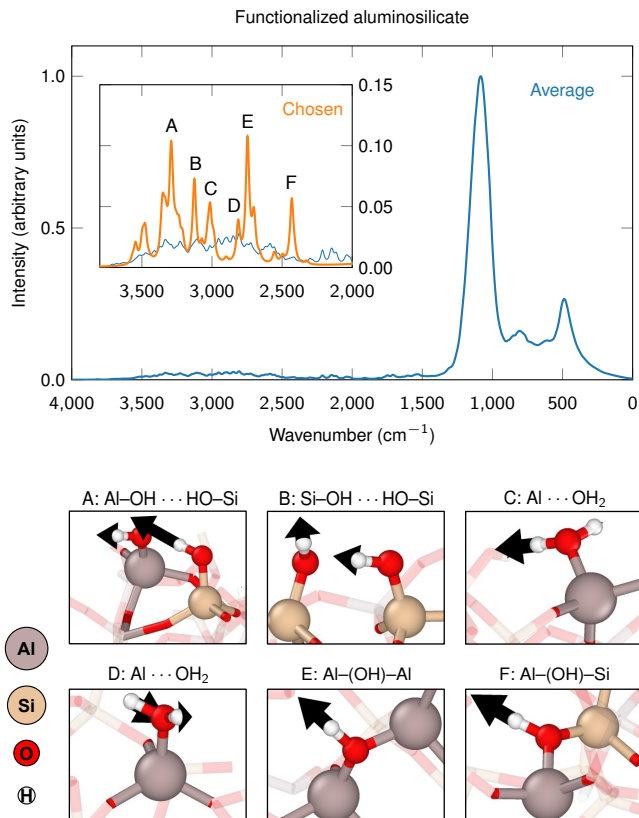


FIG. 5. Predictions with the trained MTPs and the end-to-end modeling workflow. Infrared spectra of aluminosilicates with 1.5 nm diameter pores and an Al/Si molar ratio of 0.2 are shown. Spectra from ten MD snapshots were averaged to mimic experimental conditions. One chosen snapshot is shown in the inset with an enlarged intensity scale. Six vibrational modes associated with the -OH functional groups are highlighted, with their displacement patterns visualized by black arrows in the atomic model.

acid sites. While Si-(OH)-Si groups can in principle act as Brønsted acid sites, their simulated concentration is comparatively low (0.01 nm^{-2}) due to their high reactivity (cf. dehydrogenation energies in Fig. 4b), indicating that they are likely absent under application conditions.

Resolving hydroxyl group vibrations

The surface acidity of mesoporous aluminosilicates is closely linked to the vibrational behavior of hydrogen atoms in hydroxyl groups within pores. Experimentally, these vibrational modes are challenging to resolve due to weak signals, spectral averaging, and overlap among multiple modes. To demonstrate the predictive power of the eq-MTP, we simulated infrared spectra of porous aluminosilicates under *operando* conditions, i.e., following functionalization (Fig. 5). Spectra were first averaged over ten MD snapshots sampled at 300 K to approximate experimental measurements. Apart from the Si/Al-O matrix bands below 1500 cm^{-1} (cf. Fig. 4a), the high-wavenumber region (2000 cm^{-1} to 3700 cm^{-1}) displays broad and weak features. Then, we show that analysis of a single snapshot resolves these features into distinct peaks, assignable to hydrogen vibrations in hydroxyl groups adjacent to Si or Al atoms. At higher wavenumbers, vibrations arise from hy-

droxyl groups bound to Si or extra-framework Al sites, with additional contributions from water molecules coordinated to surface Al sites. The predicted spectrum also shows that bridging Al-(OH)-Si groups are associated with low-wavenumber bands, indicating the presence of strongly acidic Brønsted sites.

DISCUSSION

A key aspect of the proposed approach is the utilization of two complementary, lightweight MLIPs. The first MLIP (referred to as syn-MLIP) is optimized for the synthesis of functionalized metallosilicate mesopores. The second MLIP (eq-MLIP) is optimized for the calculation of mesopore properties in thermodynamic equilibrium, such as vibrational spectra. This hybrid strategy is vital to achieve the best overall performance in simulating the challenging amorphous metallosilicates with functional hydroxyl groups and, optionally, with water in the pores.

Another important aspect of the proposed approach is the generation of different sizes of pores in the amorphous matrix. A repulsive cylinder potential, first introduced by Feuston,⁶⁹ ensures the formation of cylindrical pores, analogous to experimental synthesis via direct liquid crystal templating.^{68,70-72} The region outside of the cylinder, i.e., the metallosilicate matrix region, is populated with precursor molecules according to the stoichiometry of the target metallosilicates. The following melt-quench procedure then leads to an amorphous matrix containing a periodic arrangement of pores. The pores can adopt different geometrical arrangements depending on the applied periodic boundary conditions, including the hexagonal ordering typically formed in experiments.^{68,70-72} Subsequent functionalization of the surface with hydroxyl groups, as well as optional water filling, is readily incorporated within the proposed synthesis protocol.

Overall, the proposed approach enables accurate and efficient end-to-end modeling of metallosilicate mesopores. The hybrid strategy allows the use of computationally efficient MLIPs for two complementary tasks—resolving amorphous structures via synthesis and equilibrium-property evaluation. The approach provides access to large simulation models embedded with mesopores, relevant, for example, to catalysis in confined geometries.⁷³ The improved efficiency further permits simulations over extended time scales, such as those required for melt-quench processes, and across many samples to capture the statistical nature of amorphous systems. For comparison, classical force fields such as ReaxFF provide lower accuracy compared to MLIPs for related systems, as demonstrated for, e.g., zeolite-H₂O mixtures.¹⁷ On the other hand, employing the recently developed foundation or universal models^{47,74-76} for structure generation, followed by fine-tuning to achieve higher accuracy in target properties, is generally computationally very demanding and, sometimes, even prone to inaccuracies (see discussion below).

We have applied the proposed approach to aluminosilicate mesopores, utilizing MTPs at level 16 as the MLIP algorithm. For the considered system composed of Al, Si, O, and H, a level-16 MTP has 608 fitting coefficients. This amounts to a relatively efficient MLIP and, thus, offers the possibility for large-scale and long-time simulations of the mesopores. The achievable RMSEs for the syn-MTP are 16 meV/atom,

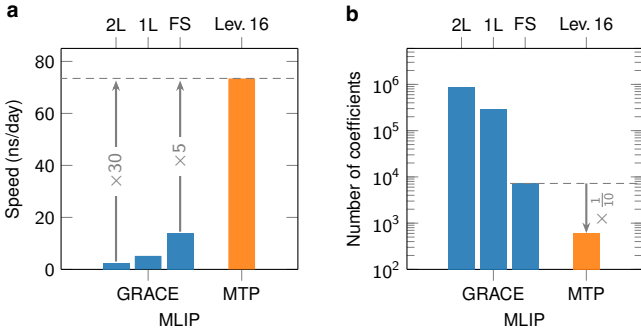


FIG. 6. Comparison of the GRACE foundation model at different complexities with an MTP of level 16. **a**, MD simulation speed. Performance was benchmarked on a 700-atom aluminosilicate model containing Si, Al, H, and O, using a single accelerator on an Nvidia V100S GPU node. Our developed MTPs are at least five times faster than the available GRACE models. **b**, Number of fitting coefficients. Our developed MTPs use at least an order of magnitude fewer fitting coefficients, resulting in substantially improved efficiency.

0.8 eV/Å, and 1.6 GPa for energies, forces, and stresses, respectively. The value of 16 meV/atom is in line with previous studies for amorphous systems using similar types of potentials, in particular, when focusing on high temperature configurations (e.g., 10 meV/atom¹⁷ or 36 meV/atom²⁰). However, it is relatively large compared to typical high-temperature RMSEs for crystalline systems (e.g., 2 meV/atom^{77–79}). Based on the proposed hybrid strategy, the RMSE values for the eq-MTP are strongly reduced, reaching values as for crystalline systems: 3 meV/atom, 0.4 eV/Å, and 0.2 GPa. In consequence of these low RMSE values, the derived materials quantities exhibit a high accuracy with respect to the underlying DFT input.

Noteworthy, energy RMSEs for the same fixed training set (same exchange-correlation functional, same DFT computational settings, same training configurations) can vary significantly. This variance can amount to several meV/atom, and it originates in different local minima in the MTP parameter space. The energy-RMSE variance propagates into a spread in the resulting target properties; however, with only a weak correlation between the two. Thus, it is crucial to use the error in the target properties in addition to the RMSEs for the validation of MTPs. A similar conclusion was drawn recently for modeling Li⁺ diffusion in solid electrolytes with MTPs.⁸⁰ For the mesoporous aluminosilicates, we have therefore provided comparisons for a wide range of target quantities (matrix density, PDF, infrared spectra, and dehydrogenation energies), referencing against available experimental data, our own measurements, and DFT calculations. The finally selected syn-MTP and eq-MTP yield a very good agreement with the reference data in their respective areas of application.

The good performance of the syn-MTP has been explicitly validated by the density and the PDF. The simulated Al-concentration-dependent density falls in absolute numbers into the range of experimental data. Likewise, the total PDF is in excellent agreement with our measured data. The eq-MTP has been explicitly validated by comparison with experimental infrared spectra for the bulk aluminosilicates. Additionally, we have validated the eq-MTP directly against the underlying DFT input for another critical target property, i.e., dehydrogenation energies. The eq-MTP predicts dehydro-

genation energies with an RMSE of 0.6 eV (10%). This is a good agreement, considering that the typically shown energy RMSE is given per atom, which then scales with the number of atoms in the system for defect/reaction energies. This error is several times lower than an RMSE of 1.68 eV that results from choosing a different DFT exchange-correlation functional (r²SCAN-D4 vs. vdW-DF-cx) and an RMSE of 1.98 eV, which is obtained from an available classical force field⁴³ (r²SCAN-D4 vs. ReaxFF).

To put the efficiency, robustness, and flexibility of the presented approach into perspective, we have presented additional results obtained with foundation models, specifically with GRACE. The density of the aluminosilicates is off by 10%; this deviation is not a failure of the GRACE model itself, but rather a materialization of the underbinding of the PBE functional to which the GRACE model was fitted to. Without refitting, the GRACE model cannot be faithfully applied to the metallocilicates. The specialized MLIPs of our approach, syn-MLIP and eq-MLIP, have been fitted to different exchange-correlation functionals, with a primary focus on r²SCAN and vdW-DF-cx, both of which show a good agreement with experimental data. A further advantage of the presented approach is computational efficiency. The level-16 MTPs developed here are faster than the fastest GRACE model by a factor of 5.25, primarily owing to an order of magnitude fewer fitting coefficients needed to represent the potential-energy surface (Fig. 6).

Application of the approach to other metallocilicates (containing, e.g., Y or Ti) requires only minor modifications with respect to what has been presented for the prototype aluminosilicates. In the initial stage before the melt-quench process, the metal oxide precursors need to be adjusted (e.g., Y₂O₃ or TiO₂). A similar adjustment is required for the metal oxide endmembers. Advantageously, part of the here published DFT training data (pure silica and/or water configurations) can be reused. The chosen DFT parameters (like the planewave cut-off) should be well applicable, and the sets of data for different exchange-correlation functionals should provide a useful starting point. Ongoing simulations on our side indeed confirm the straightforward applicability to other metallocilicates. Beyond variations in the chemical space, modifications in the geometry of the pores can be achieved by a proper adjustment of the repulsive potentials—utilized in the present study for the construction of the hexagonally arranged cylindrical pores. One such matrix geometry could be a three-dimensional network of pores.⁷¹ In yet broader terms, we expect the presented domain-specific training strategy to be suited for an end-to-end modeling of geometrically and chemically complex systems, for which the equilibrium structure is not known *a priori* and, thus, needs to be resolved *in silico*.

METHODS

A. Development of MLIPs

1. MTPs

Machine-learning interatomic potentials (MLIPs), specifically moment tensor potentials (MTPs), were trained for the two utilized exchange-correlation functionals (vdW-DF-cx and r²SCAN-D4).^{81–83} For each functional, syn-MTP was optimized for the generation of aluminosilicate mesopores by the templated melt-quench process and the description of confined

water inside the mesopores. Eq-MTP was optimized for an accurate description of the low-temperature aluminosilicate-mesopore properties with the surface functionalized by OH groups and optionally including water inside the pore. To faithfully describe the large-scale mesoporous structures using the training sets accessible with DFT calculations, a physically-informed active-learning scheme was applied, which focused on the physically relevant local environments of the structures.⁸⁴

The MTPs were fitted using the MLIP code.^{40,85} Level 16 MTPs with four species resulting in 608 parameters were used, and a cutoff distance R_{cut} of 5 Å was set. The fitting weights for energy, force, and stress were $1/N_i$, 0.01 Å^2 , and $0.001/N_i$, respectively, for N_i atoms in the i 'th configuration. The active learning scheme was performed following Ref. [86]. Different compositions and structures were used, and the MD simulations were tailored for sampling desired properties, such as stable melt-quenching processes. Additionally, configurations from *ab initio* MD trajectories were selected and added to the training set. Details of training procedures are provided in the Supporting Information.

2. DFT calculations

The energies, forces, and stresses of configurations in the training sets were calculated using density functional theory (DFT) as implemented in VASP⁸⁷ within the projector augmented-wave (PAW) method.^{88,89} The configurations of the valence electrons in the PAW potentials were: Si: $3s^2 3p^2$; O: $2s^2 2p^4$; Al: $3s^2 3p^1$; H: $1s^1$. For the exchange-correlation functional, we used a generalized gradient approximation (GGA) with van der Waals (vdW) correction, i.e., vdW-DF-cx,⁸¹ and a meta-GGA functional with vdW correction, i.e., r²SCAN-D4.^{82,83} The vdW interaction was considered due to the presence of hydrogen bonds in water and SiO₂.⁹⁰

The high-accuracy DFT calculations (high-DFT) were performed for selected snapshots with an energy cutoff of 600 eV, $1.5 \times \text{ENMAX}$ (default cutoff) for accurate stress, a \mathbf{k} -point spacing (KSPACING) of 0.52 Å^{-1} corresponding to 200 or greater kpt-atoms, and the Gaussian smearing method with a smearing width of 0.1 eV. Low-accuracy DFT (low-DFT) *NVT ab initio* MD simulations were performed with an energy cutoff of 400 eV (ENMAX). After the training set was generated by active learning with the vdW-DF-cx functional, the energies, forces, and stresses were obtained by the r²SCAN-D4 functional, unless otherwise specified.^{91,92}

B. MD simulations

1. Melt-quench processes

Bulk amorphous aluminosilicate structures with a composition of $\text{SiO}_2(\text{Al}_2\text{O}_3)_{x/2}$ for different Al/Si molar ratios x ($x = 0, 0.05, 0.1, 0.2$) were generated using a melt-quench process based on the respective syn-MTP. All simulations were performed using the LAMMPS software.^{93,94} Initial structures were generated by randomly inserting appropriate precursor molecules (SiO_2 , Al_2O_3) into a cubic box according to the experimental density^{53–57} of binary bulk amorphous aluminosilicates for a given Al/Si ratio, amounting to approximately 700 atoms for the density calculation. Afterwards, the initial structures were subjected to the melt-quench procedure,^{13,95,96} which consisted of an *NVT* heating step (300 to 5000 K, 23.5 K/ps heat rate), an *NVT* melt-equilibration step (5000 K for 200 ps), a fast *NVT* quench step (5000 K to 4000 K, 10 K/ps quench rate), a slow *NpT* quench step (4000 K to 3000 K, 5 K/ps quench rate) and an equilibration step (300 K for 250 ps).

The density of a unique bulk amorphous structure was obtained by sampling over the last 200 ps of the 300 K equilibration trajectory. For a given Al/Si ratio, the density was averaged over 50 unique amorphous configurations.

2. Aluminosilicates with pores

Porous amorphous aluminosilicates with a composition of $\text{SiO}_2(\text{Al}_2\text{O}_3)_{x/2}$ were created, similar to the bulk structures with an additional cylindrical wall inside of a hexagonal cell, similar to the approach of Feuston.⁶⁹ Initially, precursor molecules were inserted into a hexagonal cell region surrounding a Lennard-Jones cylinder wall, according to the bulk experimental density for a target Al/Si ratio. The resulting structure was subsequently subjected to

the same melt-quench procedure as for the bulk amorphous aluminosilicates using the syn-MTP.

The pores were functionalized with OH groups via formal hydroxylation⁹⁷ of bridging X-O-X groups (with $\text{X} = \text{Si}, \text{Al}$), followed by annealing at elevated temperatures. Initially, all 3-fold coordinated Si and dangling oxygen atoms on the pore surface were saturated. Afterwards, all available bridging X-O-X groups at the pore surface were hydroxylated to form two X-OH groups respectively. The surface-accessibility of X-O-X groups was determined via a modified version of the PYZEO code, considering a probe radius of 1.86 Å,^{98–100} close to that of an N_2 molecule. The resulting structures were relaxed based on the r²SCAN-D4 syn-MTP and subjected to an annealing procedure under *NpT* conditions, consisting of a heating step (300 K to 820 K, 5 K/ps heat rate), an annealing step (820 K for 2 ns), a quenching step (820 K to 300 K, 5 K/ps quench rate) and an equilibration step (320 K for 300 ps). H_2O or H_3O^+ molecules that formed from dehydroxylation of X-OH groups during relaxation or annealing were removed before being subjected to annealing or analysis.

To compare the density of surface-accessible OH groups to experimental measurements, six unique OH-functionalized aluminosilicate mesopores with an initial pore diameter of 6.1 nm, an Al/Si molar ratio of 0.2 and lattice constants of $a = 10 \text{ nm}$ and $c = 5 \text{ nm}$ were generated from different melt-quench runs. The resulting OH pore surface densities were averaged over all unique structures.

C. Validations and predictions

1. PDFs

The atomic pair distribution functions (PDFs) of bulk aluminosilicates generated using r²SCAN-D4 syn-MTPs, weighted by X-ray scattering powers, were calculated as implemented in the DIFFPY-CMI package.^{101,102} The limited range of scattering vectors of the respective instrument was simulated with $Q_{\text{max}} = 50 \text{ Å}^{-1}$.¹⁰³ For each Al/Si ratio, 5 samples of 3000-atom bulk aluminosilicates were used for the statistics. The disorder in the amorphous structures and a tiny thermal displacement $U_{\text{iso,eqiv}} = 0.001 \text{ Å}^2$ described the broadening of atomic pair distributions.

2. Dehydrogenation energies of OH groups

The dehydrogenation energies of Al-OH and Si-OH groups at the surface of OH-functionalized mesoporous aluminosilicates were obtained as the reaction energies of removal of a H atom, $E = E(\text{pore-Si/Al-O}) + E(\text{H}) - E(\text{pore-Si/Al-OH})$, where $E(\text{pore-Si/Al-O})$ is the pore with a Si- or Al-OH group, whose H was removed, H is a hydrogen atom in vacuum, and pore-Si/Al-OH is the pore with a Si- or Al-OH group. The dehydrogenation energies were obtained at the r²SCAN-D4 DFT level, and the respective eq-MTP level of theory. Since the energy of a single atom in the training set of an MTP has vanishing weight, $E(\text{H})$ for the eq-MTP was taken from r²SCAN-D4 DFT. Furthermore, a reactive force field potential (ReaxFF) was used to calculate the dehydrogenation energies, including the H energy $E(\text{H})$, as implemented in LAMMPS.⁴³ Overall, a total of 697 H atoms (single Si: 200, single Al: 185, geminal Si: 100, bridging Si-Si: 75, bridging Si-Al: 100, bridging Al-Al: 37) were analyzed across 91 unique pore structures with each pore structure containing approximately 700 atoms.

3. Infrared spectra

The infrared spectra were simulated by calculating the change in the polarization of a vibrational normal mode using the Born effective charge tensor as implemented in PHONOPY-SPECTROSCOPY.¹⁰⁴ 30 samples of 200-atom bulk aluminosilicates were generated using the melt-quench process using r²SCAN-D4 syn-MTP. 10 samples of 700-atom porous aluminosilicates with Al/Si molar ratio of 0.2 were generated, functionalized with OH groups, and annealed at 800 K for 10 ns. The generated H_2O and H_3O^+ molecules in the pores were removed. The structures were relaxed using r²SCAN-D4 eq-MTP using the LAMMPS package and the Born effective charges were calculated using the density functional perturbation theory^{105,106} at the level of GGA, vdW-DF-cx functional as implemented in VASP. The energy cutoff of 400 eV, and the Γ point for the Brillouin-zone sampling were used. To obtain

effective harmonic potentials, 200 uncorrelated snapshots per sample were generated at 20 K by *NVT* MD of the *r*²SCAN-D4 eq-MTP using LAMMPS under the Langevin thermostat with a friction parameter of 0.01 fs⁻¹. The force coefficients with a cutoff radius of 4 Å of the effective harmonic potentials were fitted using HIPHIVE¹⁰⁷ and efficient iterative algorithm for sparse linear equations as implemented in SCIPY.¹⁰⁸ The numbers of fitted parameters are 1.81×10^5 and 5.64×10^5 and the test *R*² values were 0.98 and 0.96, for the bulk and the mesoporous structures, respectively. The infrared spectra were obtained from the change in the macroscopic polarization of a vibrational mode with the linewidth of 30 cm⁻¹ using PHONOPY-SPECTROSCOPY.

4. Comparison to GRACE foundation models

The speed of graph atomic cluster expansion (GRACE) foundation models was compared with that of MTP-Kokkos¹⁰⁹ in GPU architecture. The tested GRACE models were GRACE-2L-OAM, GRACE-1L-OAM, GRACE-FS-OAM as implemented in GRACEMAKER package.^{45,110} A single accelerator on an Nvidia V100S GPU node was used. Aluminosilicates with 700 atoms were used to undergo the melt-quench process and the speed was calculated for the initial 2000 steps using LAMMPS. The number of coefficients of GRACE models were obtained by reducing the chemical complexity of foundation models to Si, Al, O, H, and counting the coefficients.

D. Synthesis of mesoporous and bulk aluminosilicates

Mesoporous aluminosilicates were synthesized according to a published protocol.⁶⁸ In short, tetramethyl orthosilicate (TMOS, Sigma Aldrich, 99.0%), Al(NO₃)₃ · 9 H₂O (Arcos Organics, ≥ 98%) and 0.1 M HNO₃ (Synergy, purum, 65%, diluted with deionized water) were mixed in a polytetrafluoroethylene flask and prepolymerized at approximately 80 mbar for 5 min while stirring. The mixture was then added to a surfactant and mixed with a KPG stirrer (Jahnke & Kunkel 1KA Labortechnik, RE16) until homogeneous. Subsequently, the clear liquid was poured on a polytetrafluoroethylene tray, left to polycondensate at 80 °C for 48 h, milled in a ball mill (Spex 800) and calcined at 550 °C for 6 h (heating rate: 1 °C·min⁻¹, air flow: 4.5 L·h⁻¹). The mass ratios of the components 0.1 M HNO₃:TMOS:Al(NO₃)₃ · 9 H₂O: surfactant were 0.710-0.432x:1:x:y, with *x* varying between 0 for silicates and 0.493 for aluminosilicates with the highest Al loading. Mesoporous materials with mesopore radii of approximately 3 nm were prepared with the Pluronic P123 (*M_n* = 5800 g·mol⁻¹, Sigma-Aldrich) as surfactant with *y* = 0.320. For mesopores with roughly 1.5 nm radius, hexadecyldimethylethylammonium bromide (≥ 98%, Sigma-Aldrich) with *y* = 0.355 was employed. No surfactant, i.e. *y* = 0, was used in the synthesis of bulk materials.

E. Sample characterization

1. TEM

Samples for transmission electron microscopy (TEM) were finely powdered and applied to polyolefin coated copper grids (mesh: 400, Plano). Measurements were performed with an EM10C/CR TEM (Zeiss) at 60 kV. Pictures were taken with a water-cooled 1k slow-scan CCD Camera (7888-IV, TRS) and the attached software Image eSP.

2. PDFs measured by synchrotron X-ray

Total scattering experiments and PDF analysis were performed as commissioned service by the Momentum Transfer GmbH. Measurements were performed at the beamline ID31 at the European Synchrotron Radiation Facility. The sample powders were loaded into cylindrical slots (approximately 1 mm thickness) held between Kapton® windows in a high-throughput sample holder. Each sample was measured in transmission with an incident X-ray energy of 75.60 keV (λ = 0.1653 Å). Measured intensities were collected using a Pilatus CdTe 2M detector (1679 × 1475 pixels, 172 × 172 μm² each) with a sample-to-detector distance of approximately 0.3 m and background corrected. NIST SRM 660b (LaB6) was used for geometry calibration performed with the software pyFAI followed by image integration including a

flat-field, geometry, solid-angle, and polarization corrections. The total scattering data was used to generate the Lorch-modified PDF data, which were normalized to the highest peak (Si–O correlation).

3. Fourier-transform infrared spectroscopy

Infrared spectra were recorded in transmission mode on a Nicolet 6700 spectrometer. Solid samples were prepared by mixing and finely grinding approximately 2 mg of the silica material with about 50 mg of pre-dried KBr (Sigma Aldrich, ≥ 90%) using a mortar and pestle, followed by pressing the mixture into pellets at a load of 2 tons. Prior to pellet preparation, the silica samples were dried under vacuum at 200 °C for 24 h to remove adsorbed water, and all sample handling and measurements were carried out in an argon-filled glove box to minimize moisture contamination.

4. Accessible hydroxyl groups

For the determination of the total amount of accessible hydroxyl groups samples were dried at 200 °C in high vacuum for 16 h to remove any adsorbed water. 30 to 50 mg of sample were weighed into a J. Young NMR tube under a dry nitrogen atmosphere together with ferrocene (10 mg, Thermo Scientific, 99%) as internal standard. Deuterated benzene (0.5 mL, Sigma Aldrich, 99.6 atom % D) and benzylmagnesium chloride in THF (0.1 mL of a 1.4 M solution, Thermo Scientific) were added and homogenized by shaking. Subsequently, the amount of formed toluene was quantified by ¹H-NMR spectroscopy (Bruker ACS 60 29 AscordTM 400 MHz). Each spectrum was acquired with eight scans with a relaxation time of 60 s to ensure quantitative signal integration.

DATA AVAILABILITY

The necessary data will be soon made available in the DaRUS Repository (darus.uni-stuttgart.de). The repository will contain the training sets (VASP OUTCAR files), and the MTPs for the aluminosilicates.

CODE AVAILABILITY

The scripts for calculations are available on request from the authors.

ACKNOWLEDGMENTS

We appreciate fruitful discussions with Yuji Ikeda, Xi Zhang, and Nikolay Zotov, the help of Konstantin Gubaev and Julian Greif in providing parts of the training sets of MTPs for silica and aluminosilicates, and the help of Ruba Ajjour and Huy Bui Duc for synthesizing some of the investigated materials. We acknowledge the European Synchrotron Radiation Facility for the provision of measurement facilities and the Momentum Transfer GmbH for performing the total scattering experiments and providing the PDF data. We appreciate the fruitful discussion of the PDF analysis with Maxwell W. Terban. This project is supported by the Deutsche Forschungsgemeinschaft (DFG, German Research Foundation) under the Collaborative Research Centres (SFB 1333, grant No. 358283783 SFB 1333/2 2022) and under Germany's Excellence Strategy (EXC 2075-390740016). This project has received funding from the European Research Council (ERC) under the European Union's Horizon 2020 research and innovation programme (grant agreement No. 865855). The authors acknowledge support by the state of Baden-Württemberg through bwHPC and the DFG through grant No. INST 40/575-1 FUGG (JUSTUS 2 cluster). B.G. and Y.O. acknowledge the support by the Stuttgart Center for Simulation Science (SimTech). The authors gratefully acknowledge the scientific support and HPC resources provided by the Erlangen National High Performance Computing Center (NHR@FAU) of the Friedrich-Alexander-Universität Erlangen-Nürnberg (FAU) under the NHR project a102cb. NHR funding is provided by federal and Bavarian state authorities. NHR@FAU hardware is partially funded by the DFG grant No. 440719683. This project is supported by the Ministry of Science, Research and the Arts Baden-Württemberg.

AUTHOR CONTRIBUTIONS

All authors designed the project, discussed the results, and wrote the manuscript. J.J., T.S., Y.O. performed the calculations, and S.I., J.B. performed experiments, M.H., N.H. discussed the analysis. B.G. and J.B. acquired funding.

ADDITIONAL INFORMATION

Competing interests: The authors declare no competing interests.

- [1] M. Fahda, J. Fayek, E. Dib, H. Cruchade, N. Pichot, N. Chaouati, L. Pinard, P. S. Petkov, G. N. Vayssilov, A. Mayoral, B. Witulski, L. Lakiss, and V. Valtchev, Investigating the physicochemical properties of an extra-large pore aluminosilicate ZEO-1, *Chem. Mater.* **36**, 5405–5421 (2024).
- [2] M. Liu, Y. Ge, J. Du, Z. Song, C. Zhang, Q. Zhou, Y. Zhang, and X. Gu, Hierarchical MFI zeolite membranes for superior xylene separation, *Adv. Funct. Mater.* **34**, 2400772 (2024).
- [3] L. Sun, G. Romolini, B. Dieu, D. Grandjean, M. Keshavarz, E. Fron, F. D’Acapito, M. B. J. Roeffaers, M. Van der Auweraer, and J. Hofkens, Ultrasensitive luminescence switching of zeolite Y confined silver clusters for dual-channel oxygen sensing, *Adv. Opt. Mater.* **12**, 2400784 (2024).
- [4] X. Liu, X. Liu, F. Yang, and Y. Wu, Experimental investigation of low-temperature fluidised bed thermochemical energy storage with salt-mesoporous silica composite materials, *Appl. Energy* **362**, 122953 (2024).
- [5] Y. Sheng and H. C. Zeng, Monodisperse aluminosilicate spheres with tunable Al/Si ratio and hierarchical macro-meso-microporous structure, *ACS Appl. Mater. Interfaces* **7**, 13578–13589 (2015).
- [6] S. H. Hakim and B. H. Shanks, Synthesis and characterization of hierarchically structured aluminosilicates, *J. Mater. Chem.* **21**, 7364–7375 (2011).
- [7] J. Gajardo, J. Colmenares-Zerpa, A. F. Peixoto, D. S. A. Silva, J. A. Silva, F. Gispert-Guirado, J. Llorca, E. A. Urqueta-Gonzalez, J. B. O. Santos, J. Szanyi, C. Sepúlveda, M. G. Álvarez, and R. J. Chimentão, Revealing the effects of high Al loading incorporation in the SBA-15 silica mesoporous material, *J. Porous Mater.* **30**, 1687 (2023).
- [8] J. Liang, Z. Liang, R. Zou, and Y. Zhao, Heterogeneous catalysis in zeolites, mesoporous silica, and metal–organic frameworks, *Adv. Mater.* **29**, 1701139 (2017).
- [9] V. L. Deringer, N. Bernstein, A. P. Bartók, M. J. Cliffe, R. N. Kerber, L. E. Marbella, C. P. Grey, S. R. Elliott, and G. Csányi, Realistic atomistic structure of amorphous silicon from machine-learning-driven molecular dynamics, *J. Phys. Chem. Lett.* **9**, 2879 (2018).
- [10] W. Li and Y. Ando, Comparison of different machine learning models for the prediction of forces in copper and silicon dioxide, *Phys. Chem. Chem. Phys.* **20**, 30006 (2018).
- [11] K. Kobayashi, H. Nakamura, A. Yamaguchi, M. Itakura, M. Machida, and M. Okumura, Machine learning potentials for tobermorite minerals, *Comput. Mater. Sci.* **188**, 110173 (2021).
- [12] S. Urata, N. Nakamura, T. Tada, A. R. Tan, R. Gómez-Bombarelli, and H. Hosono, Suppression of rayleigh scattering in silica glass by codoping boron and fluorine: Molecular dynamics simulations with force-matching and neural network potentials, *J. Phys. Chem. C* **126**, 2264 (2022).
- [13] L. C. Erhard, J. Rohrer, K. Albe, and V. L. Deringer, A machine-learned interatomic potential for silica and its relation to empirical models, *npj Comput. Mater.* **8**, 90 (2022).
- [14] D. Unruh, R. V. Meidanshahi, S. M. Goodnick, G. Csányi, and G. T. Zimányi, Gaussian approximation potential for amorphous Si : H, *Phys. Rev. Mater.* **6**, 065603 (2022).
- [15] M. Bertani, T. Charpentier, F. Faglioni, and A. Pedone, Accurate and transferable machine learning potential for molecular dynamics simulation of sodium silicate glasses, *J. Chem. Theory Comput.* **20**, 1358 (2024).
- [16] L. C. Erhard, J. Rohrer, K. Albe, and V. L. Deringer, Modelling atomic and nanoscale structure in the silicon–oxygen system through active machine learning, *Nat. Commun.* **15**, 1927 (2024).
- [17] A. Erlebach, M. Šípka, I. Saha, P. Nachtigall, C. J. Heard, and L. Grajciar, A reactive neural network framework for water-loaded acidic zeolites, *Nat. Commun.* **15**, 4215 (2024).
- [18] H. Li, Y. Jing, Z. Liu, L. Cong, J. Zhao, Y. Sun, W. Li, J. Yan, J. Yang, and X. Li, A machine-learning interatomic potential to study dry/wet oxidation process of silicon, *J. Appl. Phys.* **136**, 095302 (2024).
- [19] R. Kayano, Y. Inagaki, R. Matsubara, K. Ishida, and T. Ohkubo, Development and validation of neural network potentials for multicomponent oxide glasses, *J. Phys. Chem. C* **128**, 17686 (2024).
- [20] N. Leimeroth, J. Rohrer, and K. Albe, Structure–property relations of silicon oxycarbides studied using a machine learning interatomic potential, *J. Am. Ceram. Soc.* **107**, 6896 (2024).
- [21] M. Falgout and P. Kroll, Machine-learning interatomic potentials for pyrolysis of polysiloxanes and properties of SiCO ceramics, *J. Am. Ceram. Soc.* **107**, 7653 (2024).
- [22] S. Roy, J. P. Dürholt, T. S. Asche, F. Zipoli, and R. Gómez-Bombarelli, Learning a reactive potential for silica-water through uncertainty attribution, *Nat. Commun.* **15**, 6030 (2024).
- [23] J. P. Perdew, J. A. Chevary, S. H. Vosko, K. A. Jackson, M. R. Pederson, D. J. Singh, and C. Fiolhais, Atoms, molecules, solids, and surfaces: Applications of the generalized gradient approximation for exchange and correlation, *Phys. Rev. B* **46**, 6671–6687 (1992).
- [24] J. P. Perdew, K. Burke, and M. Ernzerhof, Generalized gradient approximation made simple, *Phys. Rev. Lett.* **77**, 3865–3868 (1996).
- [25] J. P. Perdew, A. Ruzsinszky, G. I. Csonka, O. A. Vydrov, G. E. Scuseria, L. A. Constantin, X. Zhou, and K. Burke, Restoring the density-gradient expansion for exchange in solids and surfaces, *Phys. Rev. Lett.* **100**, 136406 (2008).
- [26] J. Sun, A. Ruzsinszky, and J. P. Perdew, Strongly constrained and appropriately normed semilocal density functional, *Phys. Rev. Lett.* **115**, 036402 (2015).
- [27] J. W. Furness, A. D. Kaplan, J. Ning, J. P. Perdew, and J. Sun, Accurate and numerically efficient r^2 SCAN meta-generalized gradient approximation, *J. Phys. Chem. Lett.* **11**, 8208–8215 (2020).
- [28] S. Grimme, S. Ehrlich, and L. Goerigk, Effect of the damping function in dispersion corrected density functional theory, *J. Comput. Chem.* **32**, 1456–1465 (2011).
- [29] Y.-S. Lin, G.-D. Li, S.-P. Mao, and J.-D. Chai, Long-range corrected hybrid density functionals with improved dispersion corrections, *J. Chem. Theory Comput.* **9**, 263–272 (2013).
- [30] E. Caldeweyher, J.-M. Mewes, S. Ehlert, and S. Grimme, Extension and evaluation of the D4 London-dispersion model for periodic systems, *Phys. Chem. Chem. Phys.* **22**, 8499–8512 (2020).
- [31] K. Berland and P. Hyldgaard, Exchange functional that tests the robustness of the plasmon description of the van der Waals

- density functional, *Phys. Rev. B* **89**, 035412 (2014).
- [32] A. P. Bartók, M. C. Payne, R. Kondor, and G. Csányi, Gaussian approximation potentials: The accuracy of quantum mechanics, without the electrons, *Phys. Rev. Lett.* **104**, 136403 (2010).
- [33] T. L. Pham, H. Kino, K. Terakura, T. Miyake, and H. C. Dam, Novel mixture model for the representation of potential energy surfaces, *J. Chem. Phys.* **145**, 154103 (2016).
- [34] J. Behler and M. Parrinello, Generalized neural-network representation of high-dimensional potential-energy surfaces, *Phys. Rev. Lett.* **98**, 146401 (2007).
- [35] H. Wang, L. Zhang, J. Han, and W. E, DeePMD-kit: A deep learning package for many-body potential energy representation and molecular dynamics, *Comput. Phys. Commun.* **228**, 178–184 (2018).
- [36] L. Zhang, J. Han, H. Wang, W. A. Saidi, R. Car, and E. Weinan, End-to-end symmetry preserving inter-atomic potential energy model for finite and extended systems, in *Proceedings of the 32nd International Conference on Neural Information Processing Systems*, NIPS'18 (Curran Associates Inc., Red Hook, NY, USA, 2018) p. 4441–4451.
- [37] R. Drautz, Atomic cluster expansion for accurate and transferable interatomic potentials, *Phys. Rev. B* **99**, 014104 (2019).
- [38] K. Schütt, P.-J. Kindermans, H. E. Sauceda Felix, S. Chmiela, A. Tkatchenko, and K.-R. Müller, Schnet: A continuous-filter convolutional neural network for modeling quantum interactions, in *Advances in Neural Information Processing Systems*, Vol. 30 (Curran Associates, Inc., 2017).
- [39] K. Schütt, O. Unke, and M. Gastegger, Equivariant message passing for the prediction of tensorial properties and molecular spectra, in *Proceedings of the 38th International Conference on Machine Learning* (PMLR, 2021) p. 9377–9388.
- [40] A. V. Shapeev, Moment tensor potentials: A class of systematically improvable interatomic potentials, *Multiscale Model. Simul.* **14**, 1153 (2016).
- [41] V. Van Speybroeck, M. Bocus, P. Cnudde, and L. Vanduyfhuys, Operando modeling of zeolite-catalyzed reactions using first-principles molecular dynamics simulations, *ACS Catal.* **13**, 11455–11493 (2023).
- [42] F. Tielens, M. Gierada, J. Handzlik, and M. Calatayud, Characterization of amorphous silica based catalysts using DFT computational methods, *Catal. Today* **354**, 3 (2020).
- [43] Y. Zhang, X. Liu, A. C. T. van Duin, X. Lu, and E. J. Meijer, Development and validation of a general-purpose ReaxFF reactive force field for earth material modeling, *J. Chem. Phys.* **160**, 094103 (2024).
- [44] A. Erlebach, P. Nachtigall, and L. Grajciar, Accurate large-scale simulations of siliceous zeolites by neural network potentials, *npj Comput. Mater.* **8**, 174 (2022).
- [45] A. Bochkarev, Y. Lysogorskiy, and R. Drautz, Graph atomic cluster expansion for semilocal interactions beyond equivariant message passing, *Phys. Rev. X* **14**, 021036 (2024).
- [46] L. Barroso-Luque, M. Shuaibi, X. Fu, B. M. Wood, M. Dzamba, M. Gao, A. Rizvi, C. L. Zitnick, and Z. W. Ulissi, Open materials 2024 (OMat24) inorganic materials dataset and models, [arXiv:2410.12771 \[cond-mat.mtrl-sci\]](https://arxiv.org/abs/2410.12771) (2024).
- [47] B. Deng, P. Zhong, K. Jun, J. Riebesell, K. Han, C. J. Bartel, and G. Ceder, Chgnet as a pretrained universal neural network potential for charge-informed atomistic modelling, *Nat. Mach. Intell.* **5**, 1031–1041 (2023).
- [48] A. Forslund, J. H. Jung, Y. Ikeda, and B. Grabowski, Free-energy perturbation in the exchange-correlation space accelerated by machine learning: Application to silica polymorphs, [arXiv:2505.00789 \[cond-mat\]](https://arxiv.org/abs/2505.00789) (2025).
- [49] J. Liu, X. He, J. Z. H. Zhang, and L.-W. Qi, Hydrogen-bond structure dynamics in bulk water: insights from ab initio simulations with coupled cluster theory, *Chem. Sci.* **9**, 2065 (2018).
- [50] J. Hänsleroth, A. Flötto, M. N. Qaisrani, and C. Dreßler, Fine-tuning unifies foundational machine-learned inter-atomic potential architectures at ab initio accuracy (2025), [arXiv:2511.05337 \[physics.chem-ph\]](https://arxiv.org/abs/2511.05337).
- [51] X. Yu and C. T. Williams, Recent advances in the applications of mesoporous silica in heterogeneous catalysis, *Catal. Sci. Technol.* **12**, 5765 (2022).
- [52] Y. Wei, W. Yang, and Z. Yang, An excellent universal catalyst support-mesoporous silica: Preparation, modification and applications in energy-related reactions, *Int. J. Hydrogen Energy* **47**, 9537 (2022).
- [53] T. Hanada, Y. Bessyo, and N. Soga, Elastic constants of amorphous thin films in the systems $\text{SiO}_2\text{-Al}_2\text{O}_3$ and $\text{AlPO}_4\text{-Al}_2\text{O}_3$, *J. Non-Cryst. Solids* **113**, 213 (1989).
- [54] M. F. Ando, O. Benzine, Z. Pan, J.-L. Garden, K. Wondraczek, S. Grimm, K. Schuster, and L. Wondraczek, Boson peak, heterogeneity and intermediate-range order in binary $\text{SiO}_2\text{-Al}_2\text{O}_3$ glasses, *Sci. Rep.* **8**, 5394 (2018).
- [55] H. Morikawa, S.-I. Miwa, M. Miyake, F. Marumo, and T. Sata, Structural analysis of $\text{SiO}_2\text{-Al}_2\text{O}_3$ glasses, *J. Am. Ceram. Soc.* **65**, 78 (1982).
- [56] S. B. Khemis, L. Cormier, E. Burov, H. Montigaud, B. Baptiste, and S. Nowak, Comparative structural study of $\text{Al}_2\text{O}_3\text{-SiO}_2$ glasses and amorphous thin films, *Int. J. Appl. Glass Sci.* **15**, 212 (2024).
- [57] I. Ohira, M. Murakami, S. Kohara, K. Ohara, and E. Ohtani, Ultrahigh-pressure acoustic wave velocities of $\text{SiO}_2\text{-Al}_2\text{O}_3$ glasses up to 200 GPa, *Prog. Earth Planet. Sci.* **3**, 18 (2016).
- [58] G. Busca, Catalytic materials based on silica and alumina: Structural features and generation of surface acidity, *Prog. Mater. Sci.* **104**, 215 (2019).
- [59] V. Sanchez Escribano, G. Garbarino, E. Finocchio, and G. Busca, γ -alumina and amorphous silica-alumina: Structural features, acid sites and the role of adsorbed water, *Top. Catal.* **60**, 1554 (2017).
- [60] F. Leydier, C. Chizallet, A. Chaumonnot, M. Digne, E. Soyer, A.-A. Quoineaud, D. Costa, and P. Raybaud, Brønsted acidity of amorphous silica-alumina: The molecular rules of proton transfer, *J. Catal.* **284**, 215 (2011).
- [61] W. Hu, Q. Luo, Y. Su, L. Chen, Y. Yue, C. Ye, and F. Deng, Acid sites in mesoporous Al-SBA-15 material as revealed by solid-state NMR spectroscopy, *Microporous Mesoporous Mater.* **92**, 22 (2006).
- [62] J. E. Readman, P. M. Forster, K. W. Chapman, P. J. Chupas, J. B. Parise, and J. A. Hriljac, Pair distribution function analysis of pressure treated zeolite Na-A, *Chem. Commun.* **23**, 3383 (2009).
- [63] H. Yamada, S. Tominaka, K. Ohara, Z. Liu, T. Okubo, and T. Wakihara, Structural evolution of amorphous precursors toward crystalline zeolites visualized by an in situ X-ray pair distribution function approach, *J. Phys. Chem. C* **123**, 28419 (2019).
- [64] A. Minami, P. Hu, Y. Sada, H. Yamada, K. Ohara, Y. Yonezawa, Y. Sasaki, Y. Yanaba, M. Takemoto, Y. Yoshida, T. Okubo, and T. Wakihara, Tracking sub-nano-scale structural evolution in zeolite synthesis by in situ high-energy X-ray total scattering measurement with pair distribution function analysis, *J. Am. Chem. Soc.* **144**, 23313 (2022).
- [65] M. Okuno, N. Zotov, M. Schmücker, and H. Schneider, Structure of $\text{SiO}_2\text{-Al}_2\text{O}_3$ glasses: Combined X-ray diffraction, IR and Raman studies, *J. Non-Cryst. Solids* **351**, 1032 (2005).
- [66] M. Palencia, Functional transformation of Fourier-transform mid-infrared spectrum for improving spectral specificity by simple algorithm based on wavelet-like functions, *J. Adv. Res.* **14**, 53–62 (2018).
- [67] D. J. Lucas, L. A. Curtiss, and J. A. Pople, Theoretical study of the silicon-oxygen hydrides SiOH_n ($n=0\text{--}4$) and SiOH_n^+ ($n=0\text{--}5$): Dissociation energies, ionization energies, enthalpies of formation, and proton affinities, *J. Chem. Phys.* **99**, 6697–6703 (1993).

- [68] S. Itzighel, T. Ott, A.-K. Ströhle, H.-H. Nguyen, R. Talei, N. Ay, M. W. Terban, M. Dyballa, G. Schmitz, D. P. Estes, and J. R. Bruckner, Efficient synthesis of well-defined ordered mesoporous aluminosilicates with tailorable acidity (2025), under review.
- [69] B. P. Feuston and J. B. Higgins, Model structures for mcm-41 materials: A molecular dynamics simulation, *J. Phys. Chem.* **98**, 4459 (1994).
- [70] J. R. Bruckner, J. Bauhof, J. Gebhardt, A.-K. Beurer, Y. Traa, and F. Giesselmann, Mechanisms and intermediates in the true liquid crystal templating synthesis of mesoporous silica materials, *J. Phys. Chem. B* **125**, 3197 (2021).
- [71] V. Meynen, P. Cool, and E. Vansant, Verified syntheses of mesoporous materials, *Microporous Mesoporous Mater.* **125**, 170 (2009).
- [72] G. S. Attard, J. C. Glyde, and C. G. Göltner, Liquid-crystalline phases as templates for the synthesis of mesoporous silica, *Nature* **378**, 366 (1995).
- [73] P. Probst, M. Lindemann, J. R. Bruckner, B. Atwi, D. Wang, F. R. Fischer, M. Hogler, M. Bauer, N. Hansen, M. Dyballa, and M. R. Buchmeiser, Ring-expansion metathesis polymerization under confinement, *J. Am. Chem. Soc.* **147**, 8741 (2025).
- [74] I. Batatia, S. Batzner, D. P. Kovács, A. Musaelian, G. N. C. Simm, R. Drautz, C. Ortner, B. Kozinsky, and G. Csányi, The design space of E(3)-equivariant atom-centred interatomic potentials, *Nat. Mach. Intell.* **7**, 56–67 (2025).
- [75] H. Yang, C. Hu, Y. Zhou, X. Liu, Y. Shi, J. Li, G. Li, Z. Chen, S. Chen, C. Zeni, M. Horton, R. Pinsler, A. Fowler, D. Zügner, T. Xie, J. Smith, L. Sun, Q. Wang, L. Kong, C. Liu, H. Hao, and Z. Lu, MatterSim: A deep learning atomistic model across elements, temperatures and pressures, [arXiv:2405.04967 \[cond-mat.mtrl-sci\]](https://arxiv.org/abs/2405.04967) (2024).
- [76] C. Chen and S. P. Ong, A universal graph deep learning interatomic potential for the periodic table, *Nat. Comput. Sci.* **2**, 718–728 (2022).
- [77] A. Forslund, J. H. Jung, P. Srinivasan, and B. Grabowski, Thermodynamic properties on the homologous temperature scale from direct upsampling: Understanding electron-vibration coupling and thermal vacancies in bcc refractory metals, *Phys. Rev. B* **107**, 174309 (2023).
- [78] J. H. Jung, A. Forslund, P. Srinivasan, and B. Grabowski, Dynamically stabilized phases with full ab initio accuracy: Thermodynamics of Ti, Zr, Hf with a focus on the hcp-bcc transition, *Phys. Rev. B* **108**, 184107 (2023).
- [79] Y. Zhou, P. Srinivasan, F. Körmann, B. Grabowski, R. Smith, P. Goddard, and A. I. Duff, Thermodynamics up to the melting point in a taylor high entropy alloy: Systematic ab initio study aided by machine learning potentials, *Phys. Rev. B* **105**, 214302 (2022).
- [80] Y. Ou, Y. Ikeda, L. Scholz, S. Divinski, F. Fritzen, and B. Grabowski, Atomistic modeling of bulk and grain boundary diffusion in solid electrolyte $\text{Li}_6\text{PS}_5\text{Cl}$ using machine-learning interatomic potentials, *Phys. Rev. Mater.* **8**, 115407 (2024).
- [81] K. Berland and P. Hyldgaard, Exchange functional that tests the robustness of the plasmon description of the van der Waals density functional, *Phys. Rev. B* **89**, 035412 (2014).
- [82] J. W. Furness, A. D. Kaplan, J. Ning, J. P. Perdew, and J. Sun, Accurate and numerically efficient $r^2\text{SCAN}$ meta-generalized gradient approximation, *J. Phys. Chem. Lett.* **11**, 8208 (2020).
- [83] S. Ehlert, U. Huniar, J. Ning, J. W. Furness, J. Sun, A. D. Kaplan, J. P. Perdew, and J. G. Brandenburg, $r^2\text{SCAN-D4}$: Dispersion corrected meta-generalized gradient approximation for general chemical applications, *J. Chem. Phys.* **154**, 061101 (2021).
- [84] X. Xu, X. Zhang, E. Bitzek, S. Schmauder, and B. Grabowski, Origin of the yield stress anomaly in L_{12} intermetallics unveiled with physically informed machine-learning potentials, *Acta Mater.* **281**, 120423 (2024).
- [85] E. Podryabinkin, K. Garifullin, A. Shapeev, and I. Novikov, MLIP-3: Active learning on atomic environments with moment tensor potentials, *J. Chem. Phys.* **159**, 084112 (2023).
- [86] I. S. Novikov, K. Gubaev, E. V. Podryabinkin, and A. V. Shapeev, The MLIP package: moment tensor potentials with MPI and active learning, *Mach. Learn.: Sci. Technol.* **2**, 025002 (2020).
- [87] G. Kresse and J. Furthmüller, Efficient iterative schemes for *ab initio* total-energy calculations using a plane-wave basis set, *Phys. Rev. B* **54**, 11169 (1996).
- [88] P. E. Blöchl, Projector augmented-wave method, *Phys. Rev. B* **50**, 17953 (1994).
- [89] G. Kresse and D. Joubert, From ultrasoft pseudopotentials to the projector augmented-wave method, *Phys. Rev. B* **59**, 1758 (1999).
- [90] M. Fischer, W. J. Kim, M. Badawi, and S. Lebègue, Benchmarking the performance of approximate van der Waals methods for the structural and energetic properties of SiO_2 and AlPO_4 frameworks, *J. Chem. Phys.* **150**, 094102 (2019).
- [91] E. Caldeweyher, J.-M. Mewes, S. Ehlert, and S. Grimme, Extension and evaluation of the D4 London-dispersion model for periodic systems, *Phys. Chem. Chem. Phys.* **22**, 8499 (2020).
- [92] S. Grimme, Generally applicable atomic-charge dependent London dispersion correction DFTD4 (2025), <https://github.com/dftd4/dftd4>.
- [93] S. Plimpton, Fast parallel algorithms for short-range molecular dynamics, *J. Comput. Phys.* **117**, 1 (1995).
- [94] A. P. Thompson, H. M. Aktulga, R. Berger, D. S. Bolintineanu, W. M. Brown, P. S. Crozier, P. J. in 't Veld, A. Kohlmeyer, S. G. Moore, T. D. Nguyen, R. Shan, M. J. Stevens, J. Tranchida, C. Trott, and S. J. Plimpton, LAMMPS - a flexible simulation tool for particle-based materials modeling at the atomic, meso, and continuum scales, *Comput. Phys. Commun.* **271**, 108171 (2022).
- [95] K. Yang, X. Xu, B. Yang, B. Cook, H. Ramos, N. M. Krishnan, M. M. Smedskjaer, C. Hoover, and M. Bauchy, Predicting the Young's modulus of silicate glasses using high-throughput molecular dynamics simulations and machine learning, *Sci. Rep.* **9**, 1 (2019).
- [96] A. Nakano, R. K. Kalia, and P. Vashishta, First sharp diffraction peak and intermediate-range order in amorphous silica, *J. Non-Cryst. Solids* **171**, 157 (1994).
- [97] P. N. Wimalasiri, N. P. Nguyen, H. S. Senanayake, B. B. Laird, and W. H. Thompson, Amorphous silica slab models with variable surface roughness and silanol density for use in simulations of dynamics and catalysis, *J. Phys. Chem. C* **125**, 23418 (2021).
- [98] D. Ongari, P. G. Boyd, S. Barthel, M. Witman, M. Haranczyk, and B. Smit, Accurate characterization of the pore volume in microporous crystalline materials, *Langmuir* **33**, 14529 (2017).
- [99] T. F. Willems, C. H. Rycroft, M. Kazi, J. C. Meza, and M. Haranczyk, Algorithms and tools for high-throughput geometry-based analysis of crystalline porous materials, *Microporous Mesoporous Mater.* **149**, 134 (2012).
- [100] pyzeo: Python interface for the zeo++ package (2025), <https://github.com/nomad-coe/pyzeo>.
- [101] P. Juhás, T. Davis, C. L. Farrow, and S. J. L. Billinge, *PDFgetX3*: a rapid and highly automatable program for processing powder diffraction data into total scattering pair distribution functions, *J. Appl. Cryst.* **46**, 560 (2013).
- [102] P. Juhás, C. L. Farrow, X. Yang, K. R. Knox, and S. J. L. Billinge, Complex modeling: a strategy and software program for combining multiple information sources to solve ill posed structure and nanostructure inverse problems, *Acta Crystallogr. A* **71**, 562 (2015).

- [103] D. Prill, P. Juhás, M. U. Schmidt, and S. J. L. Billinge, Modelling pair distribution functions (PDFs) of organic compounds: describing both intra- and intermolecular correlation functions in calculated PDFs, *J. Appl. Cryst.* **48**, 171 (2015).
- [104] J. M. Skelton, L. A. Burton, A. J. Jackson, F. Oba, S. C. Parker, and A. Walsh, Lattice dynamics of the tin sulphides SnS_2 , SnS and Sn_2S_3 : vibrational spectra and thermal transport, *Phys. Chem. Chem. Phys.* **19**, 12452 (2017).
- [105] S. Baroni and R. Resta, Ab initio calculation of the macroscopic dielectric constant in silicon, *Phys. Rev. B* **33**, 7017 (1986).
- [106] M. Gajdoš, K. Hummer, G. Kresse, J. Furthmüller, and F. Bechstedt, Linear optical properties in the projector-augmented wave methodology, *Phys. Rev. B* **73**, 045112 (2006).
- [107] F. Eriksson, E. Fransson, and P. Erhart, The Hiphive package for the extraction of high-order force constants by machine learning, *Adv. Theory Simul.* **2**, 1800184 (2019).
- [108] C. C. Paige and M. A. Saunders, LSQR: An algorithm for sparse linear equations and sparse least squares, *ACM Trans. Math. Softw.* **8**, 43 (1982).
- [109] Z. Meng, K. Zongo, E. Torres, C. Maxwell, R. E. Grant, and L. K. Béland, A Kokkos-accelerated moment tensor potential implementation for LAMMPS (2025), [arXiv:2510.00193 \[cond-mat.mtrl-sci\]](#).
- [110] Y. Lysogorskiy, A. Bochkarev, and R. Drautz, Graph atomic cluster expansion for foundational machine learning interatomic potentials (2025), [arXiv:2508.17936 \[cond-mat.mtrl-sci\]](#).